

# SLAB MELTING AS A BARRIER TO DEEP CARBON SUBDUCTION

AR Thomson<sup>1,2</sup>, MJ Walter<sup>1</sup>, SC Kohn<sup>1</sup> and RA Brooker<sup>1</sup>

<sup>1</sup>*School of Earth Sciences, University of Bristol, BS8 1RJ.* <sup>2</sup>*Department of Earth Sciences, UCL, WC1E 6BT.*

**Interactions between crustal and mantle reservoirs dominate the surface inventory of volatile elements over geological time, moderating atmospheric composition and maintaining a life-supporting planet<sup>1</sup>. Whilst volcanoes expel volatile components into surface reservoirs, subduction of oceanic crust is responsible for replenishment of mantle reservoirs<sup>2,3</sup>. Many natural, ‘superdeep’ diamonds originating in the deep upper mantle and transition zone host mineral inclusions indicating an affinity to subducted oceanic crust<sup>4-7</sup>. Our experiments show that the majority of slab geotherms will intersect a deep depression along the melting curve of carbonated oceanic crust at depths of ~ 300 to 700 km, creating a barrier to direct carbonate recycling into the deep mantle. Low-degree partial melts are alkaline carbonatites that are highly reactive with reduced ambient mantle, producing diamond. Many inclusions in superdeep diamonds are best explained by carbonate melt – peridotite reaction. A deep carbon barrier may dominate the recycling of carbon in the mantle and contribute to chemical and isotopic heterogeneity of the mantle reservoir.**

Altered oceanic crust incorporates appreciable carbon, which is added by magmatic and hydrothermal processes<sup>8</sup>, and by addition of CO<sub>2</sub> during interaction of basalt with seawater<sup>9</sup>. Together, these alteration processes result in subducting lithosphere that contains an average of ~ 2 wt.% CO<sub>2</sub> in the uppermost volcanic section and 100 - 5000 ppm CO<sub>2</sub> throughout the remaining 7 km of crust<sup>8</sup>. Crustal carbon initially contains a mixture of reduced hydrocarbons<sup>8</sup> and oxidised carbonates<sup>9</sup>. However, metamorphic re-equilibration of slab carbon with ferric iron and/or oxidizing fluids produced during serpentine dehydration at sub-arc conditions, likely converts most slab carbon to carbonate<sup>10</sup>. Some of this carbon is returned to the exosphere in volcanic arcs, but both theoretical<sup>11</sup> and experimental<sup>12</sup> studies suggest that a significant quantity of carbon may survive beyond slab dehydration, and be subducted into the mantle.

Carbon is insoluble in mantle silicate minerals<sup>13</sup> and is stored either as carbonate, carbide or diamond depending on the oxidation state. Under oxidising conditions carbonate lowers the melting point (solidus) of mantle peridotite by some five hundred degrees compared with volatile-free mantle<sup>14</sup>. However, at the more reducing conditions prevailing deeper in the upper mantle and transition zone, carbon will be stored as diamond or carbide minerals<sup>15</sup>, where it does not appreciably influence melting.

35 Superdeep diamonds originate from depths beneath the lithospheric mantle ( $\geq 200$  km) and are the  
36 only direct samples of the deep mantle carbon reservoir. Inclusions in these diamonds are  
37 dominated by upper mantle and transition zone minerals, which are mostly associated with  
38 subducted mafic lithologies rather than peridotite<sup>4,7,16</sup>. Many superdeep diamonds are made of  
39 isotopically light carbon<sup>6,7</sup> and, where measured, their inclusions contain isotopically heavy  
40 oxygen<sup>17</sup>, unambiguously indicating an origin from recycled surface material<sup>6,7,17</sup>. The elevated  
41 trace element abundances of many silicate inclusions suggest crystallization from a low-degree  
42 melt, thought to be generated from melting of subducted oceanic crust<sup>7,18</sup>. Here we examine the fate  
43 of subducting carbonated MORB (mid-ocean ridge basalt) as it reaches the transition zone, and the  
44 potential for melt-mantle reactions to reproduce superdeep diamonds and their distinctive inclusion  
45 assemblages.

46  
47 Previous experimental studies have investigated the melting behaviour of carbonated basalt at  
48 elevated pressures, but only one extends beyond 10 GPa<sup>19</sup>. These studies show a remarkable  
49 diversity in melting behaviour making extrapolation to higher pressures difficult. In addition, the  
50 bulk compositions employed in previous studies often contain considerably more CO<sub>2</sub> than mean  
51 oceanic crust, and fall outside the compositional field of natural MORB rocks (see Methods, EDF1  
52 and EDT1). To better understand the melting behaviour of deeply subducted oceanic crust we have  
53 determined the melting phase relations of a synthetic MORB composition containing 2.5 wt.% CO<sub>2</sub>  
54 between 3 and 21 GPa (Methods). Our starting composition replicates the major element  
55 composition of basaltic rocks from IODP hole 1256D<sup>20</sup> and falls within the range of natural crust  
56 compositions<sup>21</sup> (EDF1).

57  
58 We observe subsolidus phase assemblages containing garnet, clinopyroxene, an SiO<sub>2</sub> polymorph,  
59 and Ti-rich oxide at all pressures. The carbon component was either CO<sub>2</sub>, dolomite, magnesite or  
60 magnesite plus Na-carbonate depending on pressure, and the positions of solid carbonate phase  
61 boundaries are consistent with previous studies<sup>22,23</sup>. Near-solidus partial melts are CO<sub>2</sub> bearing  
62 silicate melts below 7 GPa, and silica-poor calcic carbonatites above 7 GPa. The alkali component  
63 of carbonatite melts increases with pressure (EDF4), and all melts have high TiO<sub>2</sub>/SiO<sub>2</sub> (see  
64 Methods and extended data items for detailed results).

65  
66 The melting temperature of carbonated oceanic crust is tightly bracketed from  $\sim 3$  to 21 GPa (figure  
67 1). Melting temperatures increase steadily with increasing pressure until about 13 GPa, when the  
68 solidus dramatically drops over a narrow pressure interval by  $\sim 200$  °C. This drop in solidus  
69 temperature is caused by a change in clinopyroxene composition towards a more Na-rich

70 composition above 13 GPa due to dissolution of Na-poor pyroxene components into coexisting  
71 garnet. Eventually, clinopyroxene becomes so sodium-rich that a coexisting Na-carbonate mineral  
72 ( $[\text{Na}_{0.97}\text{K}_{0.03}]_{0.33}[\text{Ca}_{0.86}\text{Mg}_{0.11}\text{Fe}_{0.03}]_{0.67}\text{CO}_3$ ) stabilizes in the subsolidus assemblage, causing the  
73 depression along the solidus. The loss of Na-poor clinopyroxene component, and the extended  
74 stability of sodic clinopyroxene in the absence of an alternative Na-bearing silicate phase, is  
75 consistent with previous studies<sup>24</sup>. Above 16 GPa the solidus changes little with pressure, remaining  
76 at  $\sim 1150$  °C, consistent with the solidus observed in a sodium-rich simplified system where sodic  
77 carbonate ( $[\text{Na},\text{K}]_{0.33}\text{Ca}_{0.67}\text{CO}_3$ ) controls melting temperatures<sup>25</sup>. The major difference between this  
78 work and the previous study of carbonated MORB above 8 GPa<sup>19</sup> is the different phase assemblage  
79 resulting from the lower and more realistic  $\text{CO}_2$  and CaO contents of our bulk composition.  
80 Previous bulk compositions with higher CaO contents (EDF1 and 5) are located on the Ca-rich side  
81 of the majorite-clinopyroxene tie-line and stabilise aragonite as the carbon-hosting phase, which can  
82 incorporate considerable  $\text{Na}_2\text{O}$ . The lower  $\text{CO}_2$  content in our bulk composition results in a smaller  
83 proportion of carbonate, of which the dominant species is Na-poor magnesite. Thus, sodic  
84 clinopyroxene remains stable as an alkali-host, coexisting with stoichiometric Na-carbonate to high  
85 pressures.

86

87 The deep solidus depression in carbonated oceanic crust at uppermost transition zone conditions  
88 creates a key control on the recycling of mantle carbon. Extrapolation of the range of modern-day  
89 oceanic crustal geotherms into the transition zone<sup>26</sup> reveals that the majority of slabs will intersect  
90 our solidus for carbonated recycled MORB (figure 1), producing carbonatite melt. Given the  
91 expected temperature profile in the average subducted slab<sup>26</sup> we estimate that melting would occur  
92 to depths of at least 7 km into the crustal section. Only the coldest modern day slabs escape the  
93 solidus depression and are able to carry their carbonate cargo beyond the transition zone. If ancient  
94 slabs were hotter<sup>3</sup>, it appears likely that carbonate subduction through the transition zone and into  
95 the lower mantle has been limited throughout Earth's history. Whilst the natural variability of  
96 subducting slabs (e.g. composition, age, temperature) will have created some range in melting  
97 behaviour, the depression of the carbonated eclogite solidus will remain an efficient barrier. Thus,  
98 direct recycling of carbon into the lower mantle may have been highly restricted throughout most of  
99 Earth history, instead being redistributed throughout the upper mantle.

100

101 Carbonatitic melts are predicted to be mobile at mantle conditions due to their low viscosity and  
102 ability to wet silicate minerals<sup>27</sup>, so should percolate out of the slab and infiltrate the overlying  
103 peridotitic mantle<sup>25</sup>. Experiments suggest that below  $\sim 250$  km, ambient mantle oxygen fugacity is

104 reducing, and a free metal phase may be present in the mantle<sup>28</sup>. Under such conditions carbonate  
105 melt is unstable and will reduce to diamond plus oxygen by a ‘redox-freezing’ reaction<sup>28</sup> such as:  
106



108

109 Thus, the expulsion of carbonatite melts due to melting of oceanic crust along the solidus  
110 depression provides an ideal environment for diamond growth across a depth interval of ~ 300 –  
111 700 km. We predict that the interaction between MORB-derived carbonatite melt and ambient  
112 peridotite is capable of reproducing many of the characteristics of superdeep diamonds and the  
113 mineral inclusions that they capture from this depth interval<sup>4,5</sup>. The most common silicate minerals  
114 identified in superdeep diamonds are majorite garnet, and a titanium-bearing, calcium-silicate phase  
115 commonly interpreted as retrogressed ‘calcium perovskite’<sup>4,6,7,18</sup>. Barometric estimates of the  
116 crystallization pressures for these majorite inclusions indicate they crystallised between 10 and 16  
117 GPa<sup>5</sup>, and inclusions of calcium perovskite are constrained by their chemistry to have formed  
118 between ~ 10 and 20 GPa<sup>6,18</sup>. These pressures are remarkably consistent with the range of pressures  
119 at which slab crustal geotherms are predicted to intersect the carbonated solidus depression (figure  
120 1).

121

122 Redox reactions in the mantle are complex and involve silicates, many containing iron that exists in  
123 both ferrous ( $\text{Fe}^{2+}$ ) and ferric form ( $\text{Fe}^{3+}$ ). To test the melt-mantle interaction model we recreated  
124 the infiltration process in a second set of experiments by partially equilibrating a model slab melt  
125 with an iron-metal-bearing transition zone peridotite assemblage at 20 GPa (see Methods for  
126 details). We observe a reaction zone between the alkaline carbonatite melt and the initial peridotitic  
127 assemblage of majorite, wadsleyite, calcium-silicate perovskite and iron metal that consists of  
128 sodium-rich majoritic garnet,  $\text{Ca}[\text{Si}, \text{Ti}]\text{O}_3$  perovskite, ferrous ringwoodite ( $\text{Mg}\# \sim 75$ ),  
129 ferropericlase ( $\text{Mg}\# \sim 0.4$ ) and diamond (EDF6, 7 and EDT3). We compare the resulting mineral  
130 compositions with previous experimental data for peridotite and MORB systems to investigate  
131 whether natural inclusion assemblages might preserve a record of mineral-melt reactions.

132

133 The compositions of the majority of superdeep majoritic garnet inclusions are not typical of those  
134 expected in either peridotitic or eclogitic bulk compositions (figure 2) and instead lie between these  
135 two end-members. Kiseeva et al.<sup>16</sup> described these intermediate compositions as pyroxenitic, and  
136 suggested that the transition zone may harbour a large component of this rock type. Our results  
137 suggest an alternate explanation. In figure 2 the majoritic garnets produced during the experimental  
138 melt-mantle interaction are intermediate between peridotitic and eclogitic compositions, and cover

139 much of the range seen in the diamond inclusions. The chemical imprint imparted by the MORB-  
140 carbonatite on the peridotitic mantle is recorded in the inclusions as elevated Ca#, Na and Ti  
141 contents alongside depleted Mg#. Our experiments only demonstrate the composition of garnets  
142 produced near the beginning of melt-mantle interaction sequence, and we suggest that the  
143 intermediate character of the natural inclusions records a snap shot of the infiltration and reaction of  
144 slab-derived carbonatite melt with peridotite.

145

146 Experimental Ca-perovskites have high titanium (~ 40 - 60 mol% CaTiO<sub>3</sub>) and are essentially  
147 magnesium free, features observed throughout the global range of 'Ca-perovskite' inclusions  
148 (EDF8). Thus, our reaction experiments reproduce the unique characteristics of diamond-hosted 'Ca-  
149 perovskite' inclusions. Crystallisation by reaction between a low-degree carbonated melt and  
150 peridotite is also consistent with the extremely elevated trace element contents of diamond-hosted  
151 'Ca-perovskites' inclusions<sup>24</sup>.

152

153 Probably the most abundant inclusions in superdeep diamonds are magnesium-iron oxide  
154 ([Mg,Fe]O), which are often interpreted to indicate diamond growth in the lower mantle<sup>4</sup>. However,  
155 our experiments demonstrate that ferropericlase can be produced in reactions between carbonatitic  
156 melt and reduced mantle peridotite at upper mantle pressures rather than requiring a lower mantle  
157 origin<sup>29</sup>. Figure 3 demonstrates that natural ferropericlase inclusions are almost all iron-rich relative  
158 to ferropericlase expected in mantle peridotite, and their compositions form arrays toward higher  
159 NiO and lower Na<sub>2</sub>O with increasing magnesium number. Our experimental ferropericlase  
160 compositions lie at the end of the arrays and are iron-rich because the peridotite starting material  
161 was initially iron-saturated. We suggest that, like the majorite inclusions, the array of intermediate  
162 ferropericlase compositions record the progressive reaction of carbonatite melt and ambient mantle.

163

164 The melting phase relations of recycled oceanic crust suggest that slabs should undergo melting and  
165 loss of carbonate components in the transition zone (figure 4), a process that has considerable  
166 implications for the deep carbon cycle. The compositions of diamond-hosted inclusions provide  
167 strong evidence of this process and confirm that carbon must survive subduction beyond sub-arc  
168 dehydration reactions. We predict that carbon is rarely transported beyond the transition zone and  
169 instead refertilises the upper mantle as diamond. Oxidation of diamond-bearing mantle upon  
170 upwelling can lead to redox melting<sup>15</sup> beneath the lithosphere and contribute significantly to the  
171 generation and geochemical signature of surface lavas. This process also likely contributes to the  
172 formation of distinctive chemical and isotopic reservoirs in the mantle<sup>30</sup>. Superdeep diamonds  
173 provide a physical record of carbon recycling above subducting slabs, which can be used to infer

174 the residence time of carbon in the mantle. This residence time is regulated by rates of subduction,  
175 convective mantle upwelling and melting beneath the lithosphere, and could occur over a range of  
176 timescales, perhaps as short as tens to hundreds of millions of years, suggesting the mantle carbon  
177 cycle can be significantly more vigorous than previously estimated<sup>2,3</sup>.

178

## 179 **References**

- 180 1. Zahnle, K. *et al.* Emergence of a habitable planet. *Space Sci. Rev.* **129**, 35–78 (2007).
- 181 2. Sleep, N. H. & Zhanle, K. Carbon dioxide cycling and implications for climate on ancient Earth. *J. Geophys. Res.*  
182 **106**, 1373–1399 (2001).
- 183 3. Dasgupta, R. & Hirschmann, M. M. The deep carbon cycle and melting in Earth's interior. *Earth Planet. Sci. Lett.*  
184 **298**, 1–13 (2010).
- 185 4. Harte, B. Diamond formation in the deep mantle: the record of mineral inclusions and their distribution in relation to  
186 mantle dehydration zones. *Mineral. Mag.* **74**, 189–215 (2010).
- 187 5. Stachel, T. Diamonds from the asthenosphere and the transition zone. *Eur. J. Mineral.* **13**, 883–892 (2001).
- 188 6. Thomson, A. R. *et al.* Origin of sub - lithospheric diamonds from the Juina - 5 kimberlite (Brazil): constraints from  
189 carbon isotopes and inclusion compositions. *Contrib. to Mineral. Petrol.* **168**, 1081 (2014).
- 190 7. Bulanova, G. *et al.* Mineral inclusions in sublithospheric diamonds from Collier 4 kimberlite pipe, Juina, Brazil:  
191 subducted protoliths, carbonated melts and primary kimberlite magmatism. *Contrib. to Mineral. Petrol.* **160**, 489–  
192 510 (2010).
- 193 8. Shilobreeva, S., Martinez, I., Busigny, V., Agrinier, P. & Laverne, C. Insights into C and H storage in the altered  
194 oceanic crust: Results from ODP/IODP Hole 1256D. *Geochim. Cosmochim. Acta* **75**, 2237–2255 (2011).
- 195 9. Alt, J. & Teagle, D. The uptake of carbon during alteration of ocean crust. *Geochim. Cosmochim. Acta* **63**, 1527–  
196 1535 (1999).
- 197 10. Debret, B. *et al.* Redox state of iron during high-pressure serpentinite dehydration. *Contrib. to Mineral. Petrol.* **169**,  
198 1-18 (2015).
- 199 11. Kerrick, D. M. & Connolly, J. A. D. Metamorphic Devolatilization of Subducted Mid-Ocean Ridge Metabasalts:  
200 Implications for Seismicity, Arc Magmatism and Volatile Recycling. *Earth Planet. Sci. Lett.* **189**, 19-29 (2001).
- 201 12. Poli, S., Franzolin, E., Fumagalli, P. & Crottini, A. The transport of carbon and hydrogen in subducted oceanic  
202 crust: An experimental study to 5 GPa. *Earth Planet. Sci. Lett.* **278**, 350–360 (2009).
- 203 13. Shcheka, S.S., Wiedenbeck, M., Frost, D.J. & Keppler H. (2006) Carbon solubility in mantle minerals. *Earth*  
204 *Planet. Sci. Lett.* **245**, 730-742.
- 205 14. Ghosh, S., Ohtani, E., Litasov, K. & Terasaki, H. Solidus of carbonated peridotite from 10 to 20 GPa and origin of  
206 magnesiocarbonatite melt in the Earth's deep mantle. *Chem. Geol.* **262**, 17–28 (2009).
- 207 15. Stagno, V., Ojwang, D. O., McCammon, C. A. & Frost, D. J. The oxidation state of the mantle and the extraction of  
208 carbon from Earth's interior. *Nature* **493**, 84–8 (2013).
- 209 16. Kiseeva, E. S. *et al.* Metapyroxenite in the mantle transition zone revealed from majorite inclusions in diamonds.  
210 *Geology* **41**, 883–886 (2013).
- 211 17. Ickert, R. B., Stachel, T., Stern, R. A. & Harris, J. W. Extreme <sup>18</sup>O-enrichment in majorite constrains a crustal origin  
212 of transition zone diamonds. *Geochem. Persp. Lett.* **1**, 65-74 (2015).
- 213 18. Walter, M. J. *et al.* Primary carbonatite melt from deeply subducted oceanic crust. *Nature* **454**, 622–625 (2008).

- 214 19. Kiseeva, E. S., Litasov, K. D., Yaxley, G. M., Ohtani, E. & Kamenetsky, V. S. Melting and phase relations of  
215 carbonated eclogite at 9-21 GPa and the petrogenesis of alkali-rich melts in the deep mantle. *J. Petrol.* **54**, 1555–  
216 1583 (2013).
- 217 20. Expedition 309/312 Scientists in Teagle et al. Proceedings of the integrated Ocean Drilling Program, Volume  
218 309/312 (2009).
- 219 21. Gale, A., Dalton, C. A., Langmuir, C. H., Su, Y. & Schilling, J.-G. The mean composition of ocean ridge basalts.  
220 *Geochemistry, Geophys. Geosystems* **14**, 489–518 (2013).
- 221 22. Martin, A. M., Laporte, D., Koga, K. T., Kawamoto, T. & Hammouda, T. Experimental study of the stability of a  
222 dolomite + coesite assemblage in contact with peridotite: Implications for sediment-mantle interaction and diamond  
223 formation during subduction. *J. Petrol.* **53**, 391–417 (2012).
- 224 23. Luth, R. W. Experimental determination of the reaction aragonite + magnesite = dolomite at 5 to 9 GPa. *Contrib. to*  
225 *Mineral. Petrol.* **141**, 222–232 (2004).
- 226 24. Okamoto, K. & Maruyama, S. The Eclogite - Garnetite transformation in the MORB + H<sub>2</sub>O system. *Phys. Earth*  
227 *Planet. Inter.* **146**, 283–296 (2004).
- 228 25. Litasov, K., Shatskiy, A., Ohtani, E. & Yaxley, G. Solidus of alkaline carbonatite in the deep mantle. *Geology* **41**,  
229 79–82 (2013).
- 230 26. Syracuse, E. M., van Keken, P. E. & Abers, G. A. The global range of subduction zone thermal models. *Phys. Earth*  
231 *Planet. Inter.* **183**, 73–90 (2010).
- 232 27. Hammouda, T. & Laporte, D. Ultrafast mantle impregnation by carbonatite melts. *Geology* **28**, 283–285 (2000).
- 233 28. Rohrbach, A. & Schmidt, M. W. Redox freezing and melting in the Earth's deep mantle resulting from carbon-iron  
234 redox coupling. *Nature* **472**, 209–12 (2011).
- 235 29. Brey, G. P., Bulatov, V., Girnis, A., Harris, J. W. & Stachel, T. Ferropericlasite - a lower mantle phase in the upper  
236 mantle. *Lithos* **77**, 655–663 (2004).
- 237 30. Jackson, M. G. & Dasgupta, R. Compositions of HIMU, EM1 and EM2 from global trends between radiogenic  
238 isotopes and major elements in ocean island basalts. *Earth Planet. Sci. Lett.* **276**, 175–186 (2008).

239

240 **Acknowledgements** A.R.T acknowledges the support of NERC grant NE/J500033/1. M.J.W. and  
241 S.C.K acknowledge the support of NERC grant NE/J008583/1. We thank S. Kearns and B. Buse for  
242 their assistance performing EPMA analyses and J. Blundy for contributing ideas and expertise  
243 during discussions with the authors.

244

245 **Author Contributions** A.R.T designed, performed and analysed the experiments, gathered data  
246 from the literature and wrote the manuscript as part of his Ph.D. studies. M.J.W. and S.C.K.  
247 provided training in experimental techniques, assisted during interpretation of results, provided  
248 advice and assisted with manuscript preparation in their roles as A.R.T.'s Ph.D. supervisors. R.A.B.  
249 provided training and assistance with experimental techniques and sample preparation alongside  
250 contributing to the scientific content and preparation of the manuscript.

251

252 **Author Information** Reprints and permissions information is available at  
253 [www.nature.com/reprints](http://www.nature.com/reprints). The authors declare no competing financial interests. Correspondence  
254 and requests for materials should be addressed to A.R.T. ([a.r.thomson@ucl.ac.uk](mailto:a.r.thomson@ucl.ac.uk)).



255 **Main text figure legends**

256 **Figure 1: The melting curve of carbonated MORB (this study) compared to hot and cold**  
257 **subduction geotherms<sup>26</sup>.** The stability fields of carbon-bearing phases are identified in different  
258 colours. Experiments performed marked by filled triangles indicating their relationship to the  
259 solidus, larger symbols mark solidus brackets. The solidus ledge creates a narrow depth interval  
260 where slab temperatures intersect the melting curve, producing a focussed region of melt generation  
261 at the top of the transition zone.

262

263 **Figure 2: Composition of majoritic garnet minerals from previous experimental studies,**  
264 **inclusions in diamonds and reaction experiments (this study).** The red field outlines the  
265 approximate range of peridotitic majorite compositions, the blue field outlines the range of MORB  
266 majorites from pressures above the carbonated MORB solidus ledge ( $> \sim 9$  GPa). Data and  
267 corresponding references for this figure are provided in the online source data file.

268

269 **Figure 3: Composition of ferropericlase minerals from previous experimental studies,**  
270 **inclusions in diamonds and reaction experiments (this study).** Blue arrows indicate the  
271 compositional evolution expected as melt-mantle interactions progress. Data and corresponding  
272 references for this figure are provided in the online source data file.

273

274 **Figure 4: Schematic of the deep mantle carbon cycle as described in the text.** Arrows represent  
275 paths and estimates of the relative magnitudes of carbon fluxes. Downwelling slabs dehydrate at  
276 sub-arc depths but retain the majority of their carbon cargo. Upon reaching the transition zone they  
277 produce carbonatite melts (this study) along the solidus ledge that infiltrate [28] and react with the  
278 overlying mantle (this study). This causes diamond production, refertilisation and associated  
279 metasomatism of the surrounding mantle. The melting of recycled crust in the transition zone  
280 essentially prevents carbon transport into the lower mantle.

281

282

283 **METHODS**

284 **Starting materials.** The starting material for experiments to determine the melting phase relations  
285 of carbonated MORB (ATCM1) replicates basalts from the IODP 1256D from the Eastern Pacific  
286 Rise<sup>20</sup> (the reported composition of IODP 1256D basalts is the average of all analyses presented in  
287 table T17 of the cited issue) with an added 2.5 wt.% CO<sub>2</sub> (EDT1). This material was formed by  
288 mixing high purity SiO<sub>2</sub>, TiO<sub>2</sub>, Al<sub>2</sub>O<sub>3</sub>, FeO, MnO, MgO, Ca<sub>3</sub>(PO<sub>4</sub>)<sub>2</sub> and CaCO<sub>3</sub>, that were fired  
289 overnight at temperatures of 400 – 1000 °C, of appropriate weights in an agate mortar under  
290 ethanol. This mixture was decarbonated and fused into a crystal-free glass in a one-atmosphere tube  
291 furnace by incrementally increasing temperature from 400 to 1500 °C prior to drop quenching into  
292 water. Subsequently weighed amounts of CaCO<sub>3</sub>, Na<sub>2</sub>CO<sub>3</sub> and K<sub>2</sub>CO<sub>3</sub> were ground into the glass,  
293 introducing the alkali and CO<sub>2</sub> components. After creation the starting material was stored at 120  
294 °C to avoid absorption of atmospheric water. Starting material ATCM2 replicates the near-solidus  
295 melt composition measured in melting experiments at 20.7 GPa and 1400/1480 °C. This was  
296 created by grinding natural magnesite and synthetic siderite with high purity CaCO<sub>3</sub>, Na<sub>2</sub>CO<sub>3</sub>,  
297 K<sub>2</sub>CO<sub>3</sub>, SiO<sub>2</sub>, TiO<sub>2</sub>, Al<sub>2</sub>O<sub>3</sub> and Ca<sub>3</sub>(PO<sub>4</sub>)<sub>2</sub>. Synthetic siderite was created in a cold-seal pressure  
298 vessel experiment run at 2 kbar and 375 °C for 7 days. A double Au capsule design containing iron  
299 (II) oxalate dehydrate in the inner and a 1:1 mixture of CaCO<sub>3</sub> and SiO<sub>2</sub> in the outer capsule  
300 produced a pale beige powder confirmed as siderite using Raman spectroscopy. The material for a  
301 sandwich experiment, to ensure near-solidus melt compositions were accurately determined at 20.7  
302 GPa, was formed of a 3:1 mixture of ATCM1:ATCM2.

303

304 The transition zone peridotite mineral assemblage in reaction experiments was synthesised at 20.7  
305 GPa and 1600 °C for 8 hours from a mixture of KR4003 natural peridotite<sup>31</sup> with an added 2.5 wt.%  
306 Fe metal. In reaction runs the recovered synthetic peridotite was loaded in a second capsule,  
307 surrounded by the ATCM2 near-solidus melt composition. Additional reaction-type experiments  
308 were performed on ground mixtures of peridotite and melt compositions. In these experiments PM1  
309 pyrolite<sup>32</sup> was used as the peridotite component and mixed with ATCM2 melt in 9:1, 7:3 and 1:1  
310 weight ratios in Fe capsules. A single mixed experiment was performed in a Au capsule and used a  
311 starting mix of PM1:Fe:ATCM2 in 16:1:4 molar ratio.

312

313 **Experimental techniques.** High-pressure experiments were performed using a combination of end-  
314 loaded piston cylinder (3 GPa) and Walker-type multi anvil (5 - 21 GPa) experiments at the  
315 University of Bristol. Piston cylinder experiments employed a NaCl-pyrex assembly with a straight  
316 graphite furnace and Al<sub>2</sub>O<sub>3</sub> inner parts. Temperature was measured using type D thermocouple  
317 wires contained in an alumina sleeve and positioned immediately adjacent to the Au<sub>80</sub>Pd<sub>20</sub> sample

318 capsule that contained the powdered starting material. We assume that the temperature gradient  
319 across the entire capsule ( $< 2$  mm) was smaller than  $20\text{ }^{\circ}\text{C}^{33,34}$ . The hot piston-in technique was  
320 used with a friction correction of 3% applied to the theoretical oil pressure to achieve the desired  
321 run conditions<sup>35</sup>.

322

323 Multi-anvil experiments were performed using Toshiba F-grade tungsten carbide cubes bearing 11,  
324 8 or 4 mm truncated corners in combination with a pre-fabricated Cr-doped MgO octahedron of 18,  
325 14 or 10 mm edge length respectively. The relationship between oil-reservoir and sample pressure  
326 for each cell was calibrated at room and high temperature ( $1200\text{ }^{\circ}\text{C}$ ) by detecting appropriate room  
327 temperature phase transitions of Bi, ZnTe and GaAs and bracketing transformations of  $\text{SiO}_2$   
328 (quartz-coesite and coesite-stishovite),  $\text{Mg}_2\text{SiO}_4$  ( $\alpha$ - $\beta$  and  $\beta$ - $\gamma$ ) and  $\text{CaGeO}_3$  (garnet-perovskite).  
329 Calibrations are estimated to be accurate within  $\pm 1$  GPa. In all experiments desired run pressure  
330 was achieved using a slow, Eurotherm controlled, pressure ramp of  $\leq 50$  tonnes/hour. Experiments  
331 were heated after high pressure was reached with high-temperatures generated using stepped  
332 graphite (18/11 cell) or straight  $\text{LaCrO}_3$  furnaces (14/8 and 10/4 cells) and monitored with type C  
333 thermocouple wires. Two 10/4 experiments, performed during a period of repeated  $\text{LaCrO}_3$  heater  
334 failures, used rolled  $40\text{ }\mu\text{m}$  thick Re furnaces. Temperature was quenched by turning off the furnace  
335 power prior to a slow decompression ramp (half the rate of experiment compression) to ambient  
336 conditions. Samples were contained in Au capsules unless temperatures exceeded its thermal  
337 stability, in which case  $\text{Au}_{80}\text{Pd}_{20}$  or  $\text{Au}_{75}\text{Pd}_{25}$  capsules were used. Run durations all exceeded 600  
338 minutes and are reported in extended data tables 2 and 3. Temperature uncertainties were believed  
339 to be less than  $\pm 20, 30$  or  $50\text{ }^{\circ}\text{C}$  for 18/11, 14/8 and 10/4 cells respectively<sup>36,37</sup>.

340

341 Recovered samples were mounted longitudinally in epoxy, polished under oil and repeatedly re-  
342 impregnated with a low viscosity epoxy (Buelher EpoHeat) in order to preserve soft and water-  
343 soluble alkali carbonate components present in run products.

344

345 **Analytical techniques.** Polished and carbon coated run products were imaged in backscatter  
346 electron mode (BSE) using a Hitachi S-3500N SEM microscope with an EDAX Genesis energy  
347 dispersive spectrometer to identify stable phases and observe product textures. Subsequently,  
348 wavelength dispersive spectroscopy (WDS) was performed using the Cameca SX100 Electron  
349 Microprobe or the Field Emission Gun Jeol JXA8530F Hyperprobe at the University of Bristol to  
350 achieve high precision chemical analyses of run products. Analyses were performed using an  
351 accelerating voltage of 15 or 12 kV on the respective instruments, with a beam current of 10 nA.  
352 Calibrations were performed during each session using a range of natural mineral and metal

353 standards and were verified by analysing secondary standards (as in [6]). Silicate phases were  
354 measured using a focused electron beam whereas carbonates and melts were analysed using an  
355 incident beam defocussed up to a maximum size of 10  $\mu\text{m}$ . Count times for Na and K were limited  
356 to 10 seconds on peak and 5 seconds on positive and negative background positions. Peak count  
357 times for other elements were 20 - 40 seconds. Additional analyses of the calcium perovskite phases  
358 grown during reaction experiments, measuring only  $\text{SiO}_2$  and  $\text{MgO}$  content, were made using the  
359 Jeol instrument at 5 kV and 10 nA to ensure reported  $\text{MgO}$  contents were not influenced by  
360 secondary fluorescence from surrounding material.

361

362 The identity of experimental-produced minerals was determined using Raman spectroscopy as a  
363 fingerprint technique. Spectra were collected using a Thermo Scientific DXRxi Raman microscope  
364 equipped with an excitation laser of either 455 or 532 nm.

365

366 **Choice of bulk composition and comparison with previous studies.** Studies that investigate the  
367 alteration of oceanic crust have demonstrated that carbon incorporation does not simply occur by  
368 the addition of a single carbonate species to MORB<sup>9</sup>. It instead appears to occur by a complex  
369 amalgamation of hydrocarbon and graphite deposition related to hydrothermal fluxing above  
370 magma chambers at the mid-ocean ridge<sup>8</sup> and underwater weathering<sup>9,38-40</sup> where seawater-derived  
371  $\text{CO}_2$  reacts with leached crustal cations, often in veins. It is believed that the quantity of biotic  
372 organic carbon in the crustal assemblage is negligible compared with abiotic organic compounds  
373 and inorganic carbonates<sup>8</sup>. These processes result in a layered crustal assemblage that, in the  
374 uppermost few hundred metres can contain up to a maximum of 4 wt.%  $\text{CO}_2$  in rare cases<sup>9,39</sup> but  
375 more commonly < 2 wt.%  $\text{CO}_2$  [8, 9, 39]. Beneath 500 m depth the carbon content drops to between  
376 100 and 5000 ppm  $\text{CO}_2$  throughout the remainder of the 7 km thick basaltic section<sup>8</sup>, and is mostly  
377 organic hydrocarbon species. The upper 300 m are regularly altered and can be generally thought to  
378 have compositions similar to the altered MORB rocks analysed by Kelley et al.<sup>41</sup>. Deeper portions  
379 of the MORB crust retain their pristine MORB compositions. It is therefore apparent that  
380 carbonated eclogite bulk compositions used in previous studies, where at least 4.4 wt.%  $\text{CO}_2$  was  
381 added to an eclogite by addition of ~ 10 wt.% carbonate minerals, may not be good analogues of  
382 naturally subducting crustal sections. The compositions of these starting materials from previous  
383 studies<sup>19,42-46</sup> can be found in EDT1. We do not include the composition of the starting material  
384 used by [47] or [48] as these studies were conducted in simplified chemical systems so are not  
385 directly comparable with these natural system compositions.

386

387 However, as some of the previous studies rightly identify and discuss, the composition of deeply  
388 subducted MORB is not likely to be the same as that entering the subduction system. One process  
389 widely believed to alter the composition of downwelling MORB is sub-arc slab dehydration. PT  
390 paths of subducted slabs<sup>26</sup> can be compared with experimental studies of hydrous, carbonated and  
391 H<sub>2</sub>O-CO<sub>2</sub>-bearing eclogite compositions<sup>12,24,42,43,49</sup> and thermodynamic models<sup>11,50</sup> to conclude that  
392 slabs experience dehydration at sub-arc conditions (i.e. 1-5 GPa) but will generally not reach high  
393 enough temperatures to undergo melting. Therefore, they will by-in-large retain their carbon  
394 components although some fraction may be lost by dissolution into aqueous fluids<sup>51,52</sup>. It is believed  
395 that sub-arc dehydration is capable of removing SiO<sub>2</sub> from the subducting assemblage, and previous  
396 carbonated MORB compositions were therefore designed to be significantly silica undersaturated  
397 (relative to fresh/altered MORB)<sup>19,43-45</sup>. Whilst studies<sup>e.g. 53-56</sup> do indicate that SiO<sub>2</sub> can become  
398 soluble in H<sub>2</sub>O at high-pressures, they infer that the solubility of silica in hydrous fluids only  
399 exceeds ~ 1 wt.% at T > 900 °C at 1 GPa (higher T at higher P). In contrast, slab dehydration occurs  
400 on all prograde slab paths at T < 850 °C. Additionally, Kessel et al.<sup>57</sup> measured the composition of  
401 quenched hydrous fluids coexisting with MORB at 4 GPa and 800 °C; their data indicates a  
402 maximum of ~ 12 wt.% SiO<sub>2</sub> can dissolve in the fluid. Given that there should be considerably less  
403 than 10 wt.% H<sub>2</sub>O (more likely << 5 wt.% H<sub>2</sub>O) in subducting assemblages this suggests a  
404 maximum SiO<sub>2</sub> loss in subducting MORB lithologies of ~ 0.6 – 1.2 wt.%. The compositions used in  
405 previous studies have SiO<sub>2</sub> depletions ranging from 3 wt.% up to, more commonly, 6 – 10 wt.%  
406 SiO<sub>2</sub> relative to MORB.

407

408 We further investigated the effect of oceanic crust alteration and sub-arc dehydration on the  
409 composition of subducted MORB rocks by compiling a dataset of altered MORB<sup>41</sup> and exhumed  
410 blueschist, greenschist and eclogite facies rocks from exhumed terrains worldwide to compare them  
411 with fresh MORB<sup>21</sup>, our starting material and previous starting materials. We then assess the  
412 relevance of our starting material based on the composition of natural MORB rocks, rather than  
413 using models of the subduction process that contain few observable constraints. Results of this  
414 comparison are plotted in EDF1. This analysis confirms that relative to fresh MORB, altered  
415 MORB and exhumed crustal rocks are somewhat depleted in SiO<sub>2</sub>, up to a maximum of 6 wt.%  
416 SiO<sub>2</sub> in the most extreme case, but more commonly 0 – 3 wt.% SiO<sub>2</sub>. Thus, many previous starting  
417 materials are too silica undersaturated to be good analogues of subducting MORB. Furthermore,  
418 this analysis reveals that altered and exhumed MORB are not enriched in CaO compared with fresh  
419 MORB, if anything they actually contain lower CaO on average. In contrast, all previous starting  
420 materials are enriched in CaO compared with fresh MORB. This is because most previous studies  
421 introduced the carbon component to their experiment by adding ~ 10 wt.% calcite to an eclogite-

422 base composition. We note that SLEC1<sup>43</sup> was not created in this manner, but instead this  
423 composition falls far from the MORB field as the authors used an eclogite xenolith erupted by a  
424 Hawaiian volcano as a base material. By plotting the position of the maj-cpx join, defined by the  
425 composition of our experimental phases plotted in EDF5, onto EDF1a we demonstrate that our bulk  
426 composition (ATCM1), ALL-MORB<sup>21</sup>, the vast majority of the fresh MORB field, altered<sup>41</sup> and  
427 exhumed MORB samples fall on the CaO-poor side of this join, i.e. on the Mg+Fe rich side.  
428 Therefore, magnesite will be the stable carbonate phase in these compositions at high pressure  
429 (above dolomite breakdown). In contrast, all previous bulk compositions plot on the Ca-rich side of  
430 this join, and therefore in a different phase field to the overwhelming majority of subducted MORB.  
431 This difference causes a significant difference in the phase relations of our starting material relative  
432 to those used in previous studies.

433

434 We acknowledge that no single bulk composition can be a perfect analogue for the entire range of  
435 subducting MORB compositions, however ATCM1 is a good proxy for sections of the MORB crust  
436 between ~ 300 m and 7 km depth that have unaltered major element compositions and low CO<sub>2</sub>  
437 contents. Additionally, ATCM1 remains a better analogue for the uppermost portions of the MORB  
438 crust than starting materials employed in previous studies because its CO<sub>2</sub> content is within the  
439 range of natural rocks whilst it is also not oversaturated in CaO or over depleted in SiO<sub>2</sub>. This is  
440 despite it falling towards the SiO<sub>2</sub> rich end of the compositional spectrum of subducting MORB  
441 rocks.

442

#### 443 **Slab $fO_2$ and carbonate survival to transition zone conditions.**

444 Recent experiments have suggested that carbonate in eclogitic assemblages may be reduced to  
445 elemental carbon, either graphite or diamond, at depths shallower than 250 km<sup>58</sup>. However,  
446 subducting slab geotherms are much colder than the experimental conditions investigated by this  
447 study, and additionally they are believed contain significant ferric iron that is further increased  
448 during de-serpentinisation<sup>10</sup>. Indeed, several observations of carbonate inclusions in sub-  
449 lithospheric diamonds<sup>e.g. 6,7,59</sup> require that slab carbon remains oxidised and mobile until diamond  
450 formation, far deeper than 250 km. Given the numerous observations from natural diamond  
451 samples, the general uncertainty in the mantle's  $fO_2$  structure and the lack of any conclusive  
452 experimental evidence that subducting carbon becomes reduced prior to reaching the transition zone  
453 we posit that nearly all subducting carbon is stable as carbonate throughout the upper mantle in  
454 subducting MORB assemblages.

455

456 **Experimental Results – Carbonated MORB melting.** EDT2 presents the run conditions,  
457 durations and phase proportions in all carbonated MORB melting experiments, which are also  
458 summarised in EDF2. Phase and melt compositions are presented in the supplementary tables.  
459 Phase proportions are calculated by mass balance calculations that use the mean composition of  
460 each phase as well as the reported  $1\sigma$  uncertainty in this mean as inputs. We note that the  $1\sigma$   
461 uncertainty for some oxides in garnet and clinopyroxene minerals occasionally exceeds 1 wt.%,  
462 although it is normally much smaller than this. These large uncertainties are a function of the small  
463 crystal sizes present in some runs, and not a function of sluggish reaction kinetics. Phase proportion  
464 calculations were run in a Monte Carlo loop of 10,000 calculation cycles where a varying random  
465 error was added to each oxide in each mineral phase during each iteration. Overall the distribution  
466 of varying random errors for each oxide form a Gaussian distribution with standard deviation equal  
467 to the reported  $1\sigma$  uncertainty of measurements. The reported proportions are the numerical mean of  
468 all calculation cycles and the  $r^2$  value reports the average squared sum of residuals. Low  $r^2$  values  
469 indicate that chemical equilibrium is likely to have been achieved and that mineral and melt  
470 compositions have been accurately determined.

471

472 Representative BSE images of the polished experiments are shown in EDF3. Garnets in  
473 experiments at all pressures contain abundant  $\text{SiO}_2$  inclusions. In subsolidus experiments the  
474 number of inclusions increases and the definition of mineral boundaries deteriorates, which makes  
475 accurate analysis of garnet compositions increasingly challenging. In supersolidus runs, garnet  
476 minerals adjacent, or near to, carbonatite melt pools have well defined edges and contain fewer  
477 inclusions. However, far from quenched melts the textures of garnets remain small and pervasively  
478 filled with inclusions, indicating the influence of melt fluxing on mineral growth. With increasing  
479 pressure, garnets become increasingly majoritic, with increasing quantities of octahedral silicon.

480

481 Clinopyroxene was observed in all subsolidus experiments, as euhedral crystals that are often  
482 spatially associated with the carbon-bearing phase. Cpx abundance falls with increasing pressure  
483 and their compositions becoming increasingly dominated by sodic components (jadeite, aegerine  
484 and  $\text{NaMg}_{0.5}\text{Si}_{2.5}\text{O}_6$ ) at high pressure (EDF5). Cpx only disappears from the stable phase  
485 assemblage in supersolidus experiments at 20.7 GPa.  $\text{SiO}_2$  is observed in all runs and are small,  
486 often elongated tabular-shaped crystals. An oxide, either  $\text{TiO}_2$  at low pressure or an Fe-Ti oxide  
487 above 13 GPa (as in [24]) are observed in all subsolidus runs.

488

489 The carbon-bearing phase in subsolidus experiments changes with increasing pressure. At 3 GPa  
490  $\text{CO}_2$ , marked by the presence of voids in the polished sample, is stable. This converts to dolomite at

491 7.9 GPa, consistent with the position of the reaction  $2cs + dol = cpx + CO_2$  [22]. Beyond  $\sim 9$  GPa  
492 dolomite becomes unstable and breaks down into magnesite + aragonite<sup>23</sup>. Therefore, because the  
493 ATCM1 bulk composition lies on the Mg+Fe<sup>2+</sup>-rich side of the garnet-cpx join (EDF5 and EDF1a),  
494 magnesite replaces dolomite as the carbon host in the experimental phase assemblage. This differs  
495 from experiments in previous studies, where aragonite was dominant because bulk compositions  
496 fall on the opposite side of the garnet-cpx join. It is clear from the ternary diagrams (EDF5) that  
497 while the tie-line between garnet and cpx remains magnesite and aragonite cannot coexist in a  
498 MORB bulk composition. Finally, at pressures above 15 GPa, Na carbonate becomes stable in the  
499 subsolidus phase assemblage. This is chemographically explained by the rotation of the garnet-cpx  
500 tie-line with increasing pressure (EDF5). Its appearance can also be justified as a necessary host of  
501 sodium at increasing pressure, since aside from clinopyroxene there is no other Na-rich phase stable  
502 on the Mg+Fe side of the maj-cpx join.

503

504 The appearance of silicate melt, containing dissolved CO<sub>2</sub> (estimated by difference), defines the  
505 solidus at 3 GPa. This may initially appear to contradict the results of some previous studies, which  
506 find carbonatite melts are produced near the solidus of carbonated eclogite at pressures lower than 7  
507 GPa<sup>e.g. 43,45,46</sup>. However, this is easily explained by the differences in CO<sub>2</sub> and SiO<sub>2</sub> content used in  
508 these studies. The higher CO<sub>2</sub> and lower SiO<sub>2</sub> contents of previous studies stabilise carbonate melt  
509 to lower temperatures relative to silicate melts. Indeed, we note that our results are consistent with  
510 those of Yaxley and Green<sup>44</sup> and Hammouda<sup>42</sup> (the two previous studies with the least depleted  
511 SiO<sub>2</sub>) who also observed near solidus melts below 5 GPa were basaltic to dacitic silicate melts  
512 containing dissolved CO<sub>2</sub>. The results of Kiseeva et al.<sup>19</sup> are not entirely self-consistent, in that at  
513 some pressures between 3.5 and 5.5 GPa they observed silicate melts prior to carbonate melts (4.5  
514 and 5 GPa), whereas this relationship is sometimes reversed (5 GPa in AuPd capsules) or both melts  
515 were observed together (3.5 GPa). The observation of two immiscible melts in previous studies  
516 likely reflects the maximum CO<sub>2</sub> solubility in silicate melts. Since our bulk composition has less  
517 CO<sub>2</sub>, akin to natural rocks, we do not observe liquid immiscibility.

518

519 In all experiments above 7 GPa near-solidus melt compositions are carbonatitic and essentially  
520 silica-free. This result is notably different from [19] who reported that near solidus melts were a  
521 mixture of silicate, carbonated silicate and carbonatite melts. We believe this contrast is caused by  
522 the interpretation of experimental run textures. Whereas [19] identified regions of fine-grained  
523 material consisting of mixtures of stable phases from elsewhere in the capsule as quenched melts,  
524 we have not followed the same interpretation of these features. Although we do recognise similar  
525 features in some run products we have interpreted these features as a consequence of poor crystal



526 growth in regions far from the influence of melt fluxing. In all supersolidus experiments we  
527 observed regions of carbonatite material (typically  $< 1$  wt.%  $\text{SiO}_2$ ) that is fully segregated from  
528 surrounding silicate minerals and possesses a typical carbonate-melt quench texture (EDF3).  
529 Silicate minerals in close-proximity to these melt pools are larger than those elsewhere in the same  
530 experiment, have well-defined crystal boundaries and contain few inclusions. Therefore, we  
531 attribute the variable texture and regions of fine-grained material present in experiments to the  
532 location of melt within experiments, which has a tendency to segregate to isolated regions of  
533 capsules under influence of temperature gradients. Although melt segregation occurs in all  
534 supersolidus experiments, the efficiency of segregation and size of melt pools significantly  
535 increases with rising temperature above the solidus. EDF4 shows the highly systematic evolution of  
536 the melt compositions reported from our study with increasing pressure, strongly supporting our  
537 interpretations.

538

539 Carbonatite melts are calcic,  $\text{Ca\#} > 0.5$  ( $\text{Ca\#} = \text{Ca}/[\text{Ca}+\text{Mg}+\text{Fe}]$ ), despite subsolidus carbonates  
540 being dominated by magnesite (EDF4). Melts have high concentrations of  $\text{TiO}_2$  (typically 1 - 3.5  
541 wt.%),  $\text{P}_2\text{O}_5$  (0.4 - 1.5 wt.%) and  $\text{K}_2\text{O}$  (0.3 - 1.5 wt.%) and a variable  $\text{Mg\#}$  (0.33 - 0.7 defined as  
542  $\text{Mg}/[\text{Mg}+\text{Fe}]$ ). The alkali content of melts, strongly dominated by  $\text{Na}_2\text{O}$  due to the bulk  
543 composition, increases with pressure (from 1 to  $\sim 15$  wt.%  $\text{Na}_2\text{O}$  at 7.9 and 20.7 GPa respectively;  
544 EDF4). This increasing  $\text{Na}_2\text{O}$  content is driven by the decreasing compatibility of  $\text{Na}_2\text{O}$  in the  
545 residual mantle phase assemblages as the abundance of stable clinopyroxene falls. At 20.7 GPa the  
546 melt composition, as evidenced both by constant phase proportions and consistent melt/majorite  
547 compositions, remains constant over a temperature interval of  $\sim 350$  °C above the solidus. It is only  
548 when temperature reaches 1530 - 1600 °C (runs #16 and #31) that the silica content of the melt  
549 begins to increase (to 8.7 wt.%) and  $\text{CO}_2$  content falls as melts start to become silica-carbonatites.

550

551 One experiment (#33) aimed to verify that measured low-degree melt compositions are accurate,  
552 and are not affected by analytical problems related to the small size of melt pools, was conducted at  
553 20.7 GPa. In this experiment the abundance of carbonate melt was increased by adding a mix  
554 replicating the low degree melt composition ATCM2 to ATCM1 in a mass ratio of 1:3. If the  
555 composition of low-degree melts has been accurately determined in 'normal' experiments then this  
556 addition will have a negligible affect on phase relations or the compositions of the garnet,  $\text{SiO}_2$  or  
557 melt; it would simply increase the melt abundance. The result of this experiment has a similar  
558 texture to all other experiments, where carbonatite melt segregates to one end of the capsule and is  
559 adjacent to large, well-formed majoritic garnets. The far end of the capsule has a much smaller  
560 crystal size, crystals have ragged edges, garnets are full of inclusions and  $\text{SiO}_2$  is present along

561 grain-boundaries and triple junctions (EDF3h). Mineral and melt compositions, although not  
562 exactly identical, are similar to those measured in ‘normal’ experiments (to achieve identical  
563 compositions an iterative approach would be required that was not deemed to be necessary) thus  
564 confirming that near-solidus melt compositions have been accurately determined. The presence of  
565 fine-grained material away from segregated melt also acts to further confirm our hypothesis  
566 regarding the vital importance of melt presence for growing large crystals during experiments.

567

#### 568 **Subsolidus carbonate species at high pressure.**

569 Comparing our starting material and results with those of previous studies using ternary and  
570 quaternary projections (EDF5) reveals that it is not possible for both magnesite and aragonite to  
571 coexist alongside majorite and clinopyroxene due to stable mineral phase fields (see above). Thus,  
572 in Mg-Fe dominated compositions, such as our starting material, magnesite is the stable carbonate  
573 at high-pressure subsolidus conditions. Whereas, in Ca dominated compositions aragonite will be  
574 the stable carbonate beyond the pressure of dolomite dissociation. Natural subducting MORB  
575 compositions, which contain, at most, a similar quantity of CO<sub>2</sub> to our bulk composition<sup>11</sup>, almost  
576 all lie on the Ca-poor side of the majorite-clinopyroxene join (EDF1 and EDF5). In this situation, as  
577 our experiments demonstrate, cpx remains an important Na-host in MORB assemblages to high  
578 pressures alongside [Na,K]<sub>0.33</sub>Ca<sub>0.67</sub>CO<sub>3</sub> structured carbonate. Ca-rich compositions containing  
579 subsolidus CaCO<sub>3</sub> experience different phase relations because aragonite can dissolve significant  
580 Na<sub>2</sub>O and so is the sole Na-host in these compositions. We conclude that because the majority of  
581 natural MORB rocks fall on the Mg+Fe side of the maj-cpx join, like our bulk composition, that the  
582 phase relations determined in this study are applicable to the case of natural subduction. Therefore,  
583 the melting point depression we observe along the carbonated MORB solidus at uppermost  
584 transition zone pressures is generally applicable to subducted oceanic crust.

585

586 **Experimental Results – Melt-mantle reactions.** Without the influence of slab-derived melts the  
587 anhydrous transition zone peridotite assemblage at 20.7 GPa and 1600 °C (experiment G168 and  
588 G176) is dominated by Na-poor majorite and wadsleyite (Mg# = 0.90) (EDF6, EDT3 and  
589 supplementary tables). Upon reaction with the near solidus alkaline carbonatite defined during  
590 melting experiments, ATCM2, a clearly defined reaction zone is observed between this ambient  
591 peridotite assemblage and the infiltrating melt (EDF6). The products of this reaction are garnet  
592 containing a notable Na<sub>2</sub>X<sup>2+</sup>Si<sub>5</sub>O<sub>12</sub> majorite component, Ca(Si,Ti)O<sub>3</sub> perovskite, ringwoodite,  
593 ferropericlaase and diamond. All of these phases were identified using Raman spectroscopy (EDF7)  
594 and their compositions are presented in the supplementary tables. Raman spectroscopy alone, which  
595 was performed prior to any sample polishing using diamond-based products, confirms the creation

596 of diamond during these reactions. We have not observed diamond using SEM techniques and  
597 believe that it resides as sub-micron sized inclusions in the various reaction-product minerals where  
598 it is seen by spectroscopic methods. The experiments performed on intimately mixed powders of  
599 melt and pyrolite also form the same phase assemblages (EDT3) and mineral compositions from  
600 those runs are also presented in the supplementary tables.

601

602 We observed the reaction products as new crystals floating in the residual carbonatite melt and/or  
603 nucleated on the relics of the peridotite assemblage, thus creating zoned minerals. We have  
604 demonstrated that the composition of majorite minerals crystallising during the reactions lie  
605 between those expected for peridotitic and eclogitic minerals at a similar pressure and possibly  
606 explain intermediate-composition diamond-hosted majorites (figure 2). We suggest that the full  
607 range of intermediate inclusion compositions might be created by the gradual shift in phase  
608 compositions, from those we observe towards more peridotitic minerals as the melt composition  
609 reacts with increasing quantities of mantle material. Additionally we have shown that the  
610 compositions of calcium perovskite (EDF8) and ferropericlae (figure 3) formed during the  
611 reactions are consistent with diamond-hosted minerals of those species. Further experiments, across  
612 the solidus ledge and into the uppermost lower mantle pressure range are required to test whether  
613 melt-mantle interactions account for all diamond-hosted inclusions.

614

## 615 **References**

- 616 31. Walter, M. J. Melting of Garnet Peridotite and the Origin of Komatiite and Depleted Lithosphere. *J. Petrol.* **39**,  
617 29–60 (1998).
- 618 32. Walter, M. J., Nakamura, E., Trönes, R. G. & Frost, D. J. Experimental constraints on crystallization  
619 differentiation in a deep magma ocean. *Geochim. Cosmochim. Acta* **68**, 4267–4284 (2004).
- 620 33. Watson, E., Wark, D., Price, J. & Van Orman, J. Mapping the thermal structure of solid-media pressure  
621 assemblies. *Contrib. to Mineral. Petrol.* **142**, 640–652 (2002).
- 622 34. Schilling, F. & Wunder, B. Temperature distribution in piston-cylinder assemblies: Numerical simulations and  
623 laboratory experiments. *Eur. J. Mineral.* **16**, 7–14 (2004).
- 624 35. McDade, P. *et al.* Pressure corrections for a selection of piston-cylinder cell assemblies. *Mineral. Mag.* **66**, 1021–  
625 1028 (2002).
- 626 36. Walter, M. J., Thibault, Y., Wei, K. & Luth, R. W. Characterizing experimental pressure and temperature  
627 conditions in multi-anvil apparatus. *Can. J. Phys.* **73**, 273–286 (1995).
- 628 37. Herlund, J., Leinenweber, K., Locke, D. & Tyburczy, J. A. A numerical model for steady-state temperature  
629 distributions in solid-medium high-pressure cell assemblies. *Am. Mineral.* **91**, 295–305 (2006).
- 630 38. Nakamura, K. & Kato, Y. Carbonatization of oceanic crust by the seafloor hydrothermal activity and its  
631 significance as a CO<sub>2</sub> sink in the Early Archean. *Geochim. Cosmochim. Acta* **68**, 4595–4618 (2004).

- 632 39. Coogan, L. a. & Gillis, K. M. Evidence that low-temperature oceanic hydrothermal systems play an important role  
633 in the silicate-carbonate weathering cycle and long-term climate regulation. *Geochemistry, Geophys. Geosystems*  
634 **14**, 1771–1786 (2013).
- 635 40. Coogan, L. a. & Dosso, S. E. Alteration of ocean crust provides a strong temperature dependent feedback on the  
636 geological carbon cycle and is a primary driver of the Sr-isotopic composition of seawater. *Earth Planet. Sci. Lett.*  
637 **415**, 38–46 (2015).
- 638 41. Kelley, K. A., Plank, T., Ludden, J. & Staudigel, H. Composition of altered oceanic crust at ODP Sites 801 and  
639 1149. *Geochemistry, Geophys. Geosystems* **4**, (2003).
- 640 42. Hammouda, T. High-pressure melting of carbonated eclogite and experimental constraints on carbon recycling and  
641 storage in the mantle. *Earth Planet. Sci. Lett.* **214**, 357–368 (2003).
- 642 43. Dasgupta, R., Hirschmann, M. M. & Withers, A. C. Deep global cycling of carbon constrained by the solidus of  
643 anhydrous carbonated eclogite under upper mantle conditions. *Earth Planet. Sci. Lett.* **227**, 73–85 (2004).
- 644 44. Yaxley, G. M. & Green, D. H. Experimental demonstration of refractory carbonate-bearing eclogite and siliceous  
645 melt in the subduction regime. *Earth Planet. Sci. Lett.* **128**, 313–325 (1994).
- 646 45. Dasgupta, R., Hirschmann, M. M. & Dellas, N. The effect of bulk composition on the solidus of carbonated  
647 eclogite from partial melting experiments at 3 GPa. *Contrib. to Mineral. Petrol.* **149**, 288–305 (2005).
- 648 46. Gerbode, C. & Dasgupta, R. Carbonate-fluxed melting of MORB-like pyroxenite at 2.9 GPa and genesis of HIMU  
649 ocean Island basalts. *J. Petrol.* **51**, 2067–2088 (2010).
- 650 47. Litasov, K. & Ohtani, E. The solidus of carbonated eclogite in the system CaO-Al<sub>2</sub>O<sub>3</sub>-MgO-SiO<sub>2</sub>-Na<sub>2</sub>O-CO<sub>2</sub> to 32  
651 GPa and carbonatite liquid in the deep mantle. *Earth Planet. Sci. Lett.* **295**, 115–126 (2010).
- 652 48. Keshav, S. & Gudfinnsson, G. H. Experimentally dictated stability of carbonated oceanic crust to moderately great  
653 depths in the Earth: Results from the solidus determination in the system CaO-MgO-Al<sub>2</sub>O<sub>3</sub>-SiO<sub>2</sub>-CO<sub>2</sub>. *J. Geophys.*  
654 *Res.* **115**, B05205 (2010).
- 655 49. Molina, J. F. & Poli, S. Carbonate stability and fluid composition in subducted oceanic crust: An experimental  
656 study on H<sub>2</sub>O-CO<sub>2</sub> bearing basalts. *Earth Planet. Sci. Lett.* **176**, 295–310 (2000).
- 657 50. Connolly, J. A. D. Computation of phase equilibria by linear programming: A tool for geodynamic modeling and  
658 its application to subduction zone decarbonation. *Earth Planet. Sci. Lett.* **236**, 524–541 (2005).
- 659 51. Manning, C. E. Geochemistry: A piece of the deep carbon puzzle. *Nat. Geosci.* **7**, 333–334 (2014).
- 660 52. Ague, J. J. & Nicolescu, S. Carbon dioxide released from subduction zones by fluid-mediated reactions. *Nat.*  
661 *Geosci.* **7**, 2–7 (2014).
- 662 53. Manning, C. E. The chemistry of subduction-zone fluids. *Earth Planet. Sci. Lett.* **223**, 1–16 (2004).
- 663 54. Newton, R. C. & Manning, C. E. Quartz solubility in H<sub>2</sub>O-NaCl and H<sub>2</sub>O-CO<sub>2</sub> solutions at deep crust-upper  
664 mantle pressures and temperatures: 2-15 kbar and 500-900 °C. *Geochim. Cosmochim. Acta* **64**, 2993–3005 (2000).
- 665 55. Newton, R. C. & Manning, C. E. Solubility of enstatite + forsterite in H<sub>2</sub>O at deep crust/upper mantle conditions: 4  
666 to 15 kbar and 700 to 900 °C. *Geochim. Cosmochim. Acta* **66**, 4165–4176 (2002).
- 667 56. Newton, R. C. & Manning, C. E. Thermodynamics of SiO<sub>2</sub>-H<sub>2</sub>O fluid near the upper critical end point from quartz  
668 solubility measurements at 10 kbar. *Earth Planet. Sci. Lett.* **274**, 241–249 (2008).
- 669 57. Kessel, R., Schmidt, M., Ulmer, P. & Pettke, T. Trace element signature of subduction-zone fluids, melts and  
670 supercritical liquids at 120 - 180 km depth. *Nature* **437**, 724–727 (2005).
- 671 58. Stagno, V. *et al.* The oxygen fugacity at which graphite or diamond forms from carbonate-bearing melts in  
672 eclogitic rocks. *Contrib. to Mineral. Petrol.* **169**, 1-18 (2015).

673 59. Zedgenizov, D. A., Kagi, H., Shatsky, V. S. & Ragozin, A. L. Local variations of carbon isotope composition in  
674 diamonds from São-Luis (Brazil): Evidence for heterogenous carbon reservoir in sublithospheric mantle. *Chem.*  
675 *Geol.* **363**, 114–124 (2014).

## 676 **Extended Data Captions**

### 677 **Extended Data Figure 1: Comparison of experimental compositions with natural rocks.**

678 ‘Fresh’ MORB rocks (red field), ALL-MORB ([21]; red circle), altered MORB rocks ([41]; pale  
679 blue circles), exhumed blueschist, greenschist and/or eclogitic rocks (yellow circles) and starting  
680 material from this (dark blue circle) and previous studies (green circles) of carbonated MORB  
681 compositions. In **a** rocks altered MORB and exhumed rock compositions that fall on the Mg-Fe side  
682 of the maj-cpx join from EDF5 plot below the dashed line, compositions that lie on the Ca side of  
683 this join are plotted with as orange circles with yellow outlines or purple circles with blue outlines  
684 and sit above the dashed curve. This confirms that magnesite will be the stable carbonate phase at  
685 high pressure in vast majority of natural crustal rocks, as is the case for ATCM1. Data and  
686 corresponding references for this figure are provided in the online source data file.

687

### 688 **Extended Data Figure 2: Experimental results/phase diagram and interpreted solidus**

689 **position.** The reactions  $\text{cpx} + \text{CO}_2 = \text{dol} + 2\text{cs}$  and  $\text{dol} = \text{mag} + \text{arag}$  are from [22] and [23] respectively.  
690 The upper left curve is the anhydrous MORB solidus. N.B due to temperature gradients in  
691 experiments at 8 GPa, a small quantity of dolomite is observed coexisting with melt in one  
692 experiment above the solidus, present at the cold end of the capsule.

693

### 694 **Extended Data Figure 3: BSE images of experimental products. a** 7.9 GPa, 1250 °C, **b** 7.9 GPa,

695 1350 °C, **c** 13.1 GPa, 1350 °C, **d** 13.1 GPa, 1450 °C, **e** 20.7 GPa, 1100 °C, **f** 20.7 GPa, 1480 °C, **g**  
696 20.7 GPa, 1600 °C, **h** sandwich experiment, 20.7 GPa, 1400 °C. The scale bar in each image is 10  
697  $\mu\text{m}$ .

698

699 **Extended Data Figure 4: Composition of experimental melts from this study.** Experimental  
700 melts from selected previous studies marked with semi-transparent greyscale symbols. The effects  
701 of increasing pressure, temperature and the effect of contamination due to partial analysis of silicate  
702 minerals surrounding small melt pools are shown in **b**.

703

### 704 **Extended Data Figure 5: The composition of experimental phases from this study projected**

705 into two quaternary plots. **a** [Ca]-[Mg+Fe<sup>2+</sup>]-[Si+Ti]-[Na+K] and **b** [Mg+Fe<sup>2+</sup>]-[Ca]-[Al+Fe<sup>3+</sup>]-  
706 [Na+K]. In both diagrams the grey fields are the compositional data projected onto the basal  
707 ternary. The red field is the range of natural MORB compositions projected onto the basal ternary.

708 The yellow star plotted in the 4-component system and projected onto the basal ternary is ATCM1  
709 (our bulk composition) whilst the black stars are bulk compositions from previous studies<sup>25-27</sup>.

710

711 **Extended Data Figure 6: BSE images of reaction experiments. a, b G169 and c, d G177.** In both  
712 experiments a reaction zone and remaining carbonatite melt surrounds the unreacted peridotite  
713 region. **a** An overview of G169. **b** A close up of the reaction in G169 containing newly crystallised  
714 calcium perovskite, majorite, ferropericlasite and ringwoodite minerals. **c** A close up of the reaction  
715 products in G177, which consist of small bright calcium perovskites, new majorite that is often  
716 observed as a rim on relic peridotitic garnet and ringwoodite. **d** An overview of G177.

717

718 **Extended Data Figure 7: Raman spectra of minerals from reaction experiment G177**  
719 **measured using a blue 455 cm<sup>-1</sup> excitation laser.** The position of the main peaks in each collected  
720 spectrum have been labelled with their shift from the excitation laser in cm<sup>-1</sup>.

721

722 **Extended Data Figure 8: Comparison of diamond-hosted calcium perovskite inclusions with**  
723 **experimental mineral compositions in MgO vs Ti# space.** Data and corresponding references for  
724 this figure are provided in the online source data file.

725

726 **Extended Data Table 1: Starting materials used in this and previous studies.** Ca# =  
727 Ca/[Ca+Mg+Fe]. Mg# = Mg/[Mg+Fe].

728

729 **Extended Data Table 2: Summary of run conditions and products for carbonated MORB**  
730 **melting experiments.** Mass balance calculations were performed as described in the supplementary  
731 information. Mineral abbreviations are as follows: gt = garnet; cpx = clinopyroxene; cs = coesite;  
732 rut = rutile; maj = majoritic garnet; st = stishovite; FeTi oxide = iron-titanium-rich oxide phase; SM  
733 = silicate melt; CM = carbonatite melt; dol = dolomite; mag = magnesite; Na carb = sodic  
734 carbonate. Phase proportions are in wt. %.

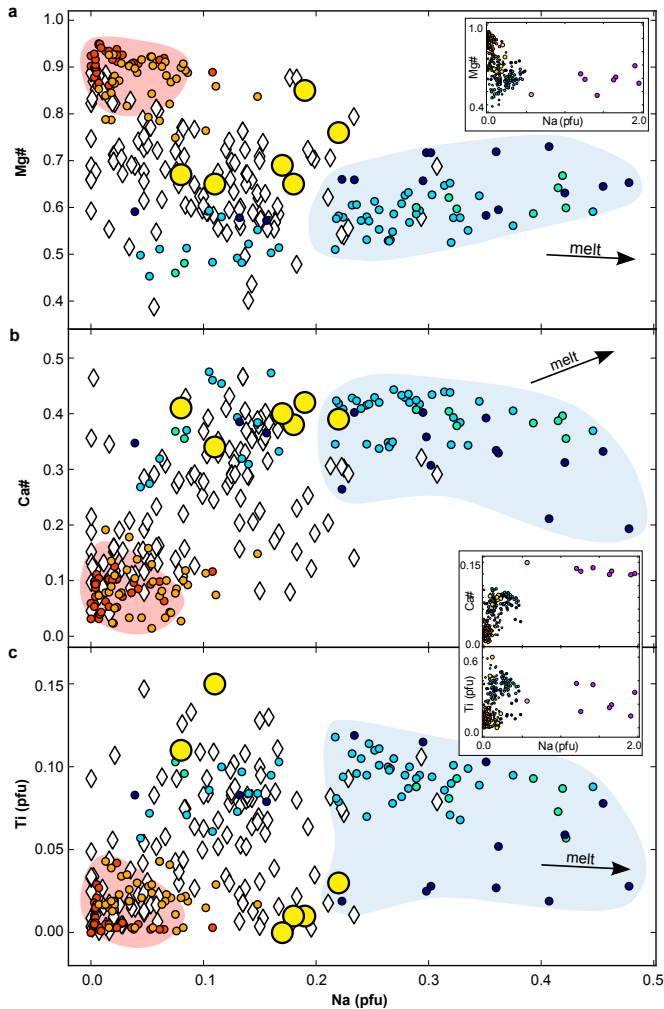
735

736 **Extended Data Table 3: Summary of reaction experiments run conditions and experimental**  
737 **products**

738

739





majorite from experiments on:

- |  |   |
|--|---|
| <span style="color: orange;">●</span> peridotite                   | <span style="border: 1px solid black; display: inline-block; width: 1em; height: 1em; vertical-align: middle;"></span> inclusions in diamonds                         |
| <span style="color: yellow;">●</span> peridotite + CO <sub>2</sub> | <span style="background-color: yellow; border: 1px solid black; display: inline-block; width: 1em; height: 1em; vertical-align: middle;"></span> reaction experiments |
| <span style="color: darkblue;">●</span> MORB                       | <span style="background-color: pink; border: 1px solid black; display: inline-block; width: 1em; height: 1em; vertical-align: middle;"></span> MORB melt 15.3 GPa     |
| <span style="color: cyan;">●</span> MORB + CO <sub>2</sub>         | <span style="background-color: purple; border: 1px solid black; display: inline-block; width: 1em; height: 1em; vertical-align: middle;"></span> MORB melt 20.7 GPa   |
| <span style="color: green;">●</span> MORB + H <sub>2</sub> O       |   |



